Coupled ITG/TEM-ETG Gyrokinetic Simulation

J. Candy and R.E. Waltz

General Atomics, San Diego, CA

e-mail contact of main author: candy@fusion.gat.com

Abstract. This work reports on the first realistic numerical studies of small-scale electron-temperature-gradient (ETG) turbulence embedded in large-scale ion-temperature-gradient *plus* trapped-electron-mode turbulence. To begin with, we find that the simplified adiabatic-ion model of ETG does not always saturate nonlinearly, suggesting that nonadiabatic (gyrokinetic) ions are required for robust saturated states of electron energy flux. Our results also qualitatively confirm a prediction of Holland and Diamond that the back-reaction of ETG on ITG turbulence is insignificant. For the parameters studied we also find that – as a mechanism for ETG turbulence supression – ITG modulation of the electron temperature gradient appears to dominate ITG random shearing. An important practical result of this work is the finding that nearly all of the electron energy transport arises from ion scales; for the Cyclone base case parameters, only 5% of the energy diffusivity, χ_e, arises from the spectral region $k_\theta \rho_i > 1.0$.

1. Introduction

The original gyrokinetic studies of electron-temperature-gradient (ETG) turbulence [1, 2, 3] used the so-called adiabatic ion model (ETG-ai), for which the perturbed ion response (in particle not gyrocenter coordinates) is approximated by

$$\frac{\delta f_i}{n_i F_M} = -\frac{z_i e \, \delta\phi(\mathbf{x}, t)}{T_i} \quad . \tag{1}$$

This result can be formally obtained in the limit $\mathcal{G}_i \to 0$, where $\mathcal{G}_i$ is the ion gyroaverage operator. The simulations reported in Refs. [1], [2] and [3] showed that, according to this model, significant transport at electron scales could occur. For the Cyclone base case [4] parameters, the electron energy diffusivity was found to be in the range $\chi_e/\chi_{\mathrm{GB}e} \sim 30$, where $\chi_{\mathrm{GB}e} \doteq \rho_e^2 v_e/a$ is the electron gyroBohm unit of diffusivity, $v_e = \sqrt{T_e/m_e}$ is the electron thermal velocity, and ρ_e is the electron gyroradius. It was further noted that the transport at moderate shear ($s = 0.8$) was dramatically higher that at weak or negative shear. We remark that subsequent particle-in-cell (PIC) simulations for essentially the same case found much lower transport levels, in the range $\chi_e/\chi_{\mathrm{GB}e} \sim 3$. However, these controversial results were soon discredited after it was discovered that discrete particle noise [5] causes the energy flux to spuriously drop to very low levels.

All numerical results in the present paper are derived from simulations with the GYRO[1] code [6]. We use where possible the same parameters (the Cyclone case case [4]) as in previous local studies; namely, a simple unshifted-circle equilibrium with $q = 1.4$, $s = 0.786$, $r/a = 0.5$, $R/a = 2.775$, $a/L_{Te} = 2.484$, $a/L_{ne} = 0.8$, $n_e = n_i$ and $T_e = T_i$. Unlike the original work of Jenko and Dorland, particle trapping (finite-r/R) is retained. Due to computational limitations and a cost-scaling of approximately $\mu^{3.5}$, where $\mu = \sqrt{m_i/m_e}$, we present results only for $\mu = 20$ and $\mu = 30$. Note that $\rho_i = \mu\rho_e$,

---

[1]For complete documentation and access to source code, see `fusion.gat.com/comp/parallel`.

$k_\theta \rho_i = \mu k_\theta \rho_e$ and $v_i = v_e/\mu$, where ρ_i is the ion gyroradius and v_i is the ion thermal velocity.

In what follows, we will refer to three types of simulations:

1. **ETG-ai**: ions are assumed to be *adiabatic*;

2. **ETG-ki**: ions are *gyrokinetic* with $a/L_{ni} = a/L_{Ti} = 0.1$;

3. **ETG-ITG**: ions are *gyrokinetic* with $a/L_{ni} = a/L_{ne}$ and $a/L_{Ti} = a/L_{Te}$.

The first model (ETG-ai) has been historically favoured in the computational community because of its simplicity; in fact, with the exception of a single axisymmetric term in the Poisson equation, it is structurally identical to the adiabatic electron model of ion-temperature-gradient (ITG) modes. The second model (ETG-ki) retains the proper long-wavelength zonal flow physics of the true physical problem without introducing ITG drive at long wavelengths. The third model (ETG-ITG) is the most realistic and includes full electron and ion dynamics.

Finally, we remark that all simulations in this paper use a 128-point velocity-space resolution (8 energies, 8 pitch angles and two signs of velocity). The parallel resolution is taken to be 10 points per passing particle orbit. These choices have been carefully studied and justified in previous work [7]. The details of the perpendicular resolution, characterized by $L_r \doteq 2\pi/(k_r)_{\min}$ and $L_\theta \doteq 2\pi/(k_\theta)_{\min}$, are given in each case. Here, "min" refers to the minimum nonzero value of the respective wavenumber.

2. Revisiting the ETG-ai model

After a great number of grid-resolution tests, it became apparent that the ETG-ai model is poorly behaved for the nominal Cyclone base case parameters (at finite r/R). To illustrate the weakness of the model, a magnetic shear scan over the range $0.1 \leq s \leq 0.8$ is shown Fig. 1a, with the high values of χ_e for the ETG-ai model (red curve) in the interval $s > 0.4$ indicative of a state which is not physically saturated. This shear scan was then repeated using the more sophisticated ETG-ki model (black curve). Remarkably, at low values of shear ($s < 0.4$), the ETG-ai model compares favourably with the more comprehensive ETG-ki model. Yet, in the region of higher shear where the ETG-ai model fails, the ETG-ki cases saturate properly with the simulations behaving robustly and in a completely familiar fashion. A comparison of (the spectral density of) the fluctuation intensity at $s = 0.3$, as shown in Fig. 1b, indicates that the spectra are overlapping except at long wavelength, where the ETG-ki model experiences a weaker intensity *pile-up* at $k_\theta \rho_e = 0$. Here I is defined as $I \doteq (e\delta\phi/T)^2$. The overall higher level of the ETG-ki simulation at small but finite wavelength (for example, near $k_\theta \rho_e = 0.1$ or equivalently, $k_\theta \rho_i = 2$) is consistent with larger ETG-ki growth rates (a stronger TEM instability) there. This effect similarly accounts for the overall greater ETG-ki transport in the $s < 0.4$ interval.

3. ETG simulations with gyrokinetic ions ($\mu = 20$)

Knowing that the ETG-ai model is unreliable, we carried out subsequent simulations using only gyrokinetic ions. Simulations using gyrokinetic ions are extremely expensive, not only because of the enormous set of wavenumbers which are coupled nonlinearly, but also due to the need to carry out ion gyroaverages in real space on a tiny electron-scale
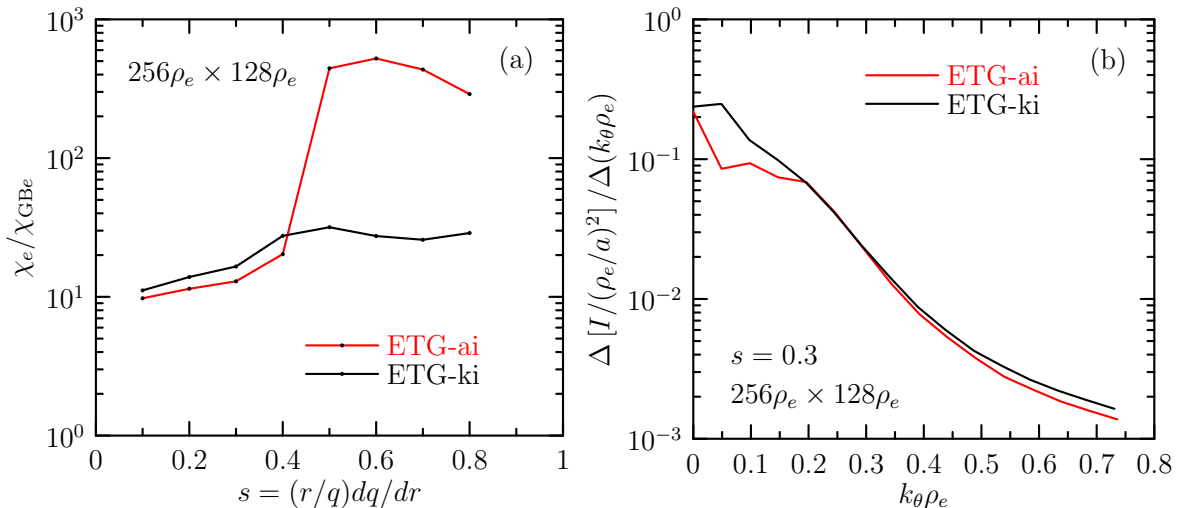
FIG. 1. *(a) Magnetic shear scan, comparing the ETG-ai model (red curve) with ETG-ki model with $\mu = 20$ (black curve). The ETG-ki model saturates in the region $s > 0.4$ where the ETG-ai model does not. (b) Sample comparison of intensities $I \doteq (e\delta\phi/T)^2$ (the time- and radial-average value at the outboard midplane $\theta = 0$) between models for $s = 0.3$. All runs used a $L_r \times L_\theta = 256\rho_e \times 128\rho_e$ box with $\Delta r/\rho_e = 2$ and $k_\theta\rho_e < 0.73$.*

grid. Furthermore, in such simulations, the sparse structure of the matrix associated with the Poisson equation is largely lost. We performed numerous resolution tests in order to develop strategies to reduce the overall computational cost. Presently, we shall describe some of these tests. In Fig. 2a, it can be seen that large-box, coarse-grid ETG-ki simulations (blue curve; $64\rho_i \times 64\rho_i$, $k_\theta\rho_e < 0.48$) exhibit good spectral overlap with small-box, fine-grid runs (black curve; $26\rho_i \times 13\rho_i$, $k_\theta\rho_e < 0.76$). This result lends confidence to the assumption that it is sufficient to simulate only the region $k_\theta\rho_e < 0.48$.

Perhaps the most important theoretical discovery of the paper is illustrated in Fig. 2b, which compares the shape of the χ_e spectrum for the ETG-ki and ETG-ITG models. Specifically, the effect of turning on ITG drive (ETG-ITG) is to reduce the high-$k_\perp$ ETG transport while at the same time increasing the low-$k_\perp$ ITG/TEM transport. To quantify the high-$k_\perp$ decrease, we sum over the interval $k_\theta\rho_e > 0.1$ to find that $\chi_e/\chi_{\text{GB}e} = 9.8$ (ETG-ki) is reduced to $\chi_e/\chi_{\text{GB}e} = 3.7$ (ETG-ITG). Regarding the low-$k_\perp$ increase, we sum over the interval $k_\theta\rho_i < 1.0$ to find $\chi_e/\chi_{\text{GB}i} = 1.2$ (ETG-ki) is increased to $\chi_e/\chi_{\text{GB}i} = 2.3$ (ETG-ITG). The increase in long-wavelength transport is consistent with an ITG branch that is stable in the ETG-ki model but unstable in the ETG-ITG model. Note that in the ETG-ki simulations, it is the TEM that is unstable at long wavelength. The puzzling feature of the results, however, is the decrease in short-wavelength transport. A comparison of the average RMS zonal flow ($k_\theta = 0$) shearing rates gives $\langle\phi''_{\text{ETG}-\text{ki}}\rangle_t/\langle\phi''_{\text{ETG}-\text{ITG}}\rangle_t \sim 1.06$, suggesting that flow shear is *not* the mechanism leading to short-wavelength stabilization. Here, the angle brackets $\langle\cdot\rangle_t$ denote a time average – normally taken over the latter half of a full simulation. In Fig. 3a, it is shown that the fluctuation intensity follows the same trend as χ_e, suggesting that the high-$k_\perp$ stabilization is a robust feature of the turbulence and not simply a peculiarity of the energy flux. Figure 3b compares the linear growth rates and quasilinear response function [8], R_e, between the two models as a function of $k_\theta\rho_i$. Here, the function R_e is related to the heat
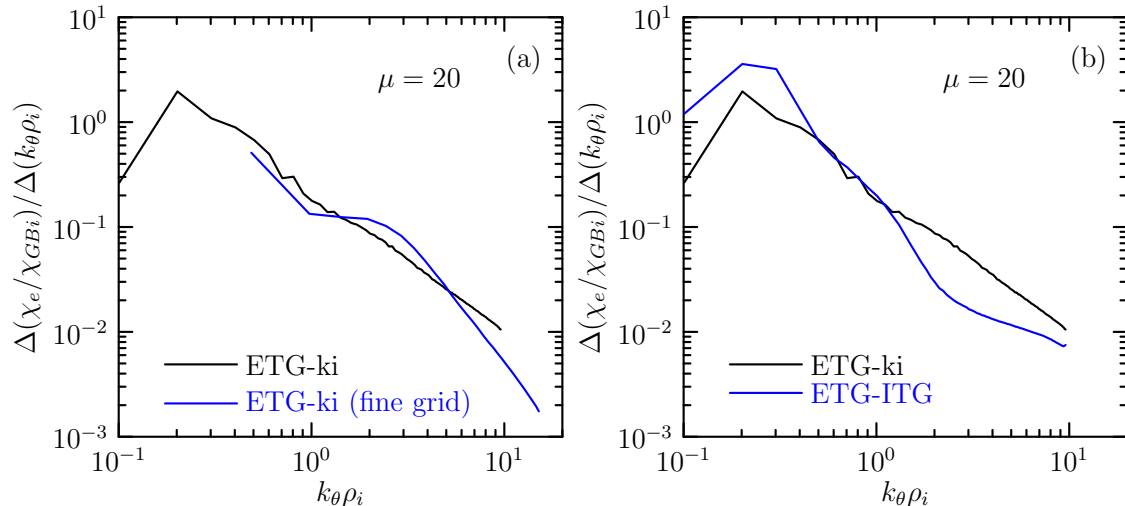
FIG. 2. (a) Comparison of ETG-ki simulations at different perpendicular resolutions: $(64\rho_i \times 64\rho_i, k_\theta\rho_e < 0.48)$ in black versus $(26\rho_i \times 13\rho_i, k_\theta\rho_e < 0.76)$ in blue. Good spectral overlap is observe, justifying the wavenumber cutoff at $k_\theta\rho_e < 0.48$ in the black curve. (b) Illustration of the effect of turning on ion gradients (ETG-ITG model). The most striking effect is the reduction of ETG transport for $k_\theta\rho_i > 1$.

flux, Q_e, at a given k_θ according to

$$(R_e)_{k_\theta} \doteq \frac{(Q_e)_{k_\theta}}{k_\theta\rho_i |\phi_{k_\theta}|^2 n_e T_e} \tag{2}$$

The curves of R_e in Fig. 3b show that the ETG-ki model tends to give greater long-wavelength transport than the ETG-ITG model for a given fluctuation intensity. This feature is corroborated by the disparity in long-wavelength intensities in Fig. 3a, which is greater than the disparity in energy diffusivities (or equivalently, fluxes) in Fig. 2b. However, at short wavelength, the values of R_e merge and the intensity curves virtually match the χ_e curves. Also, the linear growth rates for the ETG-ki model are greater than for the ETG-ITG model past the region at $k_\theta\rho_i \sim 0.4$ where the latter model jumps from the ITG to TEM branch. This is consistent with the nonlinear results of Fig. 2b. A accompanying nonlinear effect is illustrated in Fig. 4, where significant electron temperature oscillations (corrugations) are seen to develop. Such corrugations are real phenomena and have been discussed in previous work [9, 10]. In the present case, these corrugations are substantially larger for the ETG-ITG model than for the ETG-ki model, suggesting that ITG modulation of the electron temperature gradient is also a candidate for the short-wavelength stabilization (as opposed to the destabilization predicted in Ref. [11]) observed in the ETG-ITG model.

We can further examine the sensitivity of the ETG-ITG results to changes in resolution. Figure 5a shows that resolving only up to $k_\theta\rho_i < 1.1$ is sufficient to describe the bulk of the electron transport. The lip at the maximum simulated $k_\theta\rho_i$ (black curve) is a familiar numerical artifact that folds downward as the grid is refined. This result confirms the prediction of Holland and Diamond [11]; namely, that the back-reaction of ETG on ITG turbulence should be weak. Next, regarding box size, Fig. 5b shows that halving the box size in each dimension does not affect the ETG-scale transport (in fact, it has remarkably little effect). Thus, in this case, a relatively cheap $L_r \times L_\theta = 32\rho_i \times 32\rho_i$ simulation (1/4 the cost of a $64\rho_i \times 64\rho_i$ run) is enough to capture the total ETG contribution
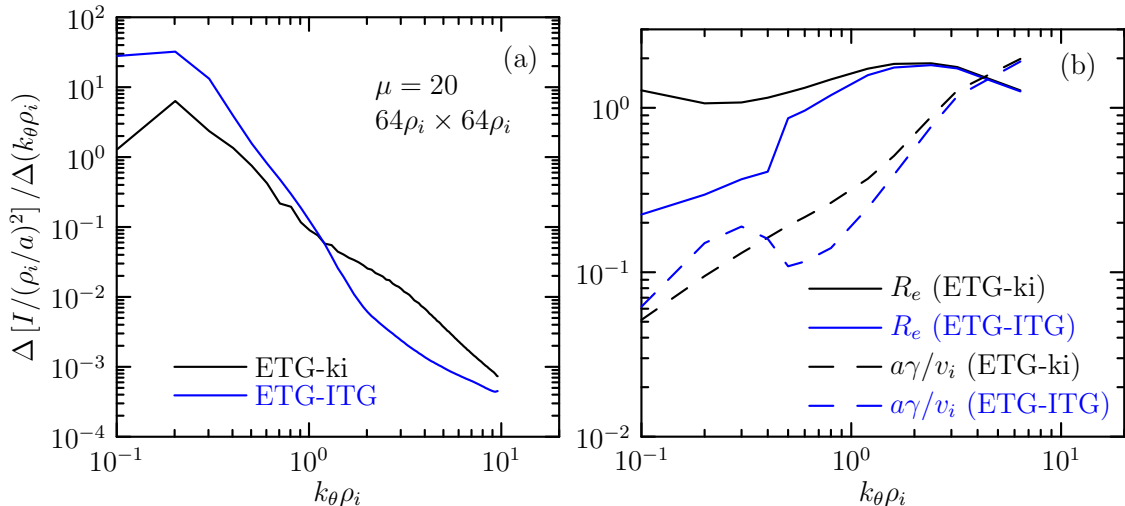
FIG. 3. (a) Analog of Fig. 2b, showing that fluctuation intensity (like transport) for the ETG-ITG model (blue) is also stronger at long wavelength and weaker at short wavelength than for the ETG-ki (black) model. (b) Curves of quasilinear heat-flux response-functions R_e as defined in Eq. 2 (solid curves), and linear growth rates (dashed curves) for the ETG-ki model (black) and ETG-ITG model (blue).

to the electron heat transport for $k_\theta \rho_i > 1$. Moreover, taken together, the black curves in each of the two panels in Fig. 5 map out the spectral shape of the more computationally expensive blue curve. This result motivates the following operational definition of ETG transport: **ETG energy transport, or χ_e^{ETG}, can be defined as that fraction of χ_e which occupies the spectral interval $k_\theta \rho_i > 1$.**

It is of experimental interest to examine the shape of the time-averaged density power-spectrum, $\langle N \rangle_t$ at the outboard midplane, where

$$N(k_r, k_\theta) \doteq \left(\frac{a}{\rho_i}\right)^2 \left|\frac{\delta n_e}{n_0}\right|^2_{k_r, k_\theta, \theta=0} . \tag{3}$$

The simulation results, plotted in Fig. 6 show that $\langle N \rangle_t$ is relatively isotropic for the ETG-ki model, and remarkably so for the ETG-ITG case. The results also imply that the fluctuation spectrum is monotonically decreasing in the ETG-range $k_\theta \rho_i > 1.0$. This result runs somewhat contrary to the prior intuitive notion that a local maximum in the ETG-range of the spectrum of χ_e, or perhaps $\delta n_e / n_e$, would occur in the vicinity of $k_\theta \rho_e \sim 0.2$ as it does in ITG turbulence at $k_\theta \rho_i \sim 0.2$.

4. Mass-ratio variation: $\mu = 20$ versus $\mu = 30$.

The aim of this section is to examine the robustness of previous conclusions to an increase in μ (toward more realistic values). First, we remark that the simulations for $\mu = 30$ are substantially more expensive than for $\mu = 20$. Indeed, the $\mu = 20$ case took 5 days on the Cray X1E[2] using 192 MSPs, whereas the $\mu = 30$ case took the same 5 days using 720 MSPs. This is consistent with a cost scaling of approximately $\mu^{3.5}$.

To begin with, in Fig. 7a, we compare electron transport as measured in ion units. We remark that the drop in χ_e at ion-scales is well-known from previous experience. For

---

[2]See info.nccs.gov/resources/phoenix. for more details.
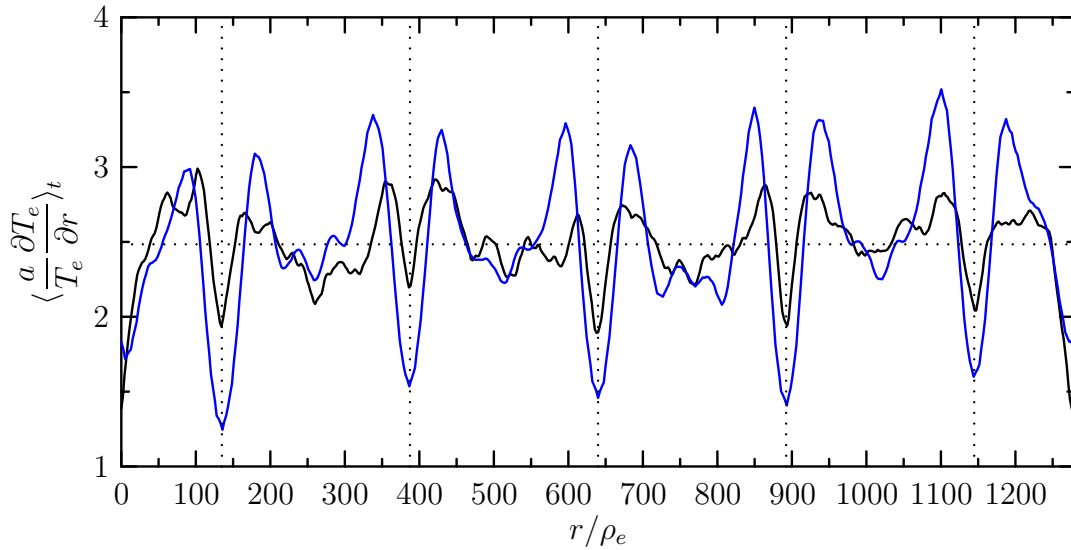
FIG. 4. Time-averaged electron temperature gradient, $\langle \partial T_e / \partial r \rangle_t$, exhibiting corrugations in both the ETG-ki (black) and ETG-ITG (blue) models. The ETG-ITG corrugations are significantly larger than those in the ETG-ki model. Vertical dotted lines give locations of lowest-order rational surfaces.
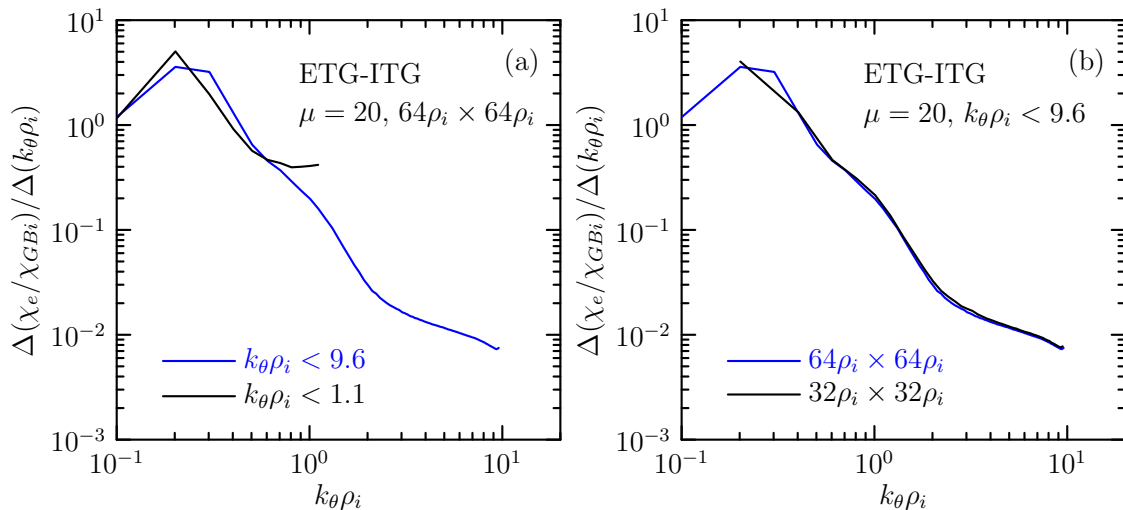
FIG. 5. (a) Blue curve is the same as in Fig. 2b. Black curve shows the effect of reduced wavenumber resolution ($k_\theta \rho_i < 1.1$) and increased radial grid spacing ($\Delta r / \rho_i = 0.67$). This results shows that very coarse perpendicular grids make an error only at the finest simulated wavelengths. (b) Blue curve is the same as in Fig. 2b. Black curve shows that halving the box size in both perpendicular dimensions leaves the short wavelength transport invariant.
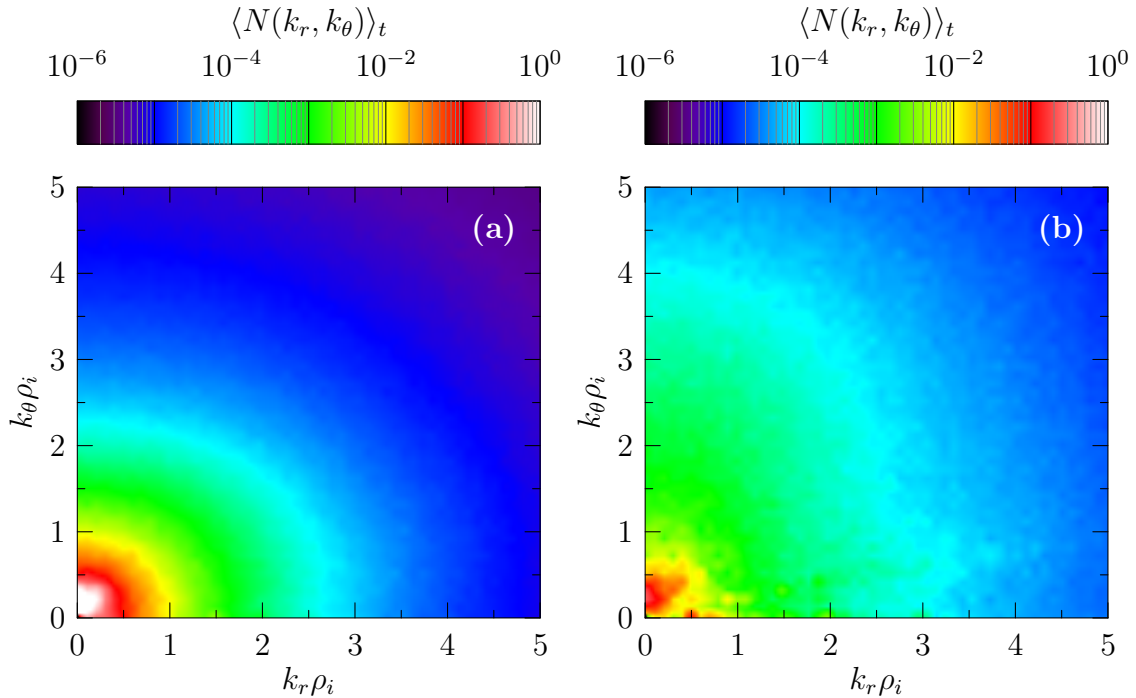
FIG. 6. (a) Time-averaged density power-spectrum, $\langle f \rangle_t$, as defined in Eq. (3), at the outboard midplane for the ETG-ITG simulation (blue curve in Fig. 5). (b) Same as in (a), but for the ETG-ki simulation (black curve in Fig. 2). Intensity scale is logarithmic.

the Cyclone base case [4] we know the drop in χ_e from $\mu = 20$ to $\mu = 30$ is comparable to the drop from $\mu = 30$ to $\mu = 60$. We tabulate various transport coefficients summed over selected intervals in $k_\theta \rho_i$ in Table 1. Still focusing on Fig. 7a, we further note that the drop in transport at electron scales is expected based on electron gyroBohm scaling; indeed, in the limit $\mu_i \to \infty$, we expect the high-$k_\perp$ contribution to $\chi_e / \chi_{\mathrm{GBe}}$ to approach a universal constant. To this end, Fig. 7b measures electron transport in electron units. Here, it is clearly see that the curve takes on a μ-independent shape for $k_\theta \rho_e > 0.1$. Quantitatively, we find that in the range $k_\theta \rho_e > 0.1$, $\chi_e / \chi_{\mathrm{GBe}} = 3.67$ at $\mu = 20$ whereas $\chi_e / \chi_{\mathrm{GBe}} = 3.76$ at $\mu = 30$. This result is also tabulated in Table 1.

Table 1. Mass-ratio dependence in ETG-ITG model for $L_r \times L_\theta = 64\rho_i \times 64\rho_i$.

	μ	$k_\theta \rho_i < 1$	$k_\theta \rho_i > 1$	$k_\theta \rho_i > 2$	$k_\theta \rho_e > 0.1$
$\chi_i / \chi_{\mathrm{GB}i}$	20	7.378	0.054	0.011	
	30	7.754	0.043	0.009	
$\chi_e / \chi_{\mathrm{GB}i}$	20	2.278	0.367	0.183	
	30	1.587	0.296	0.157	
$D / \chi_{\mathrm{GB}i}$	20	-0.81	0.134	0.009	
	30	-1.60	0.074	0.010	
$\chi_e / \chi_{\mathrm{GB}e}$	20				3.67
	30				3.76
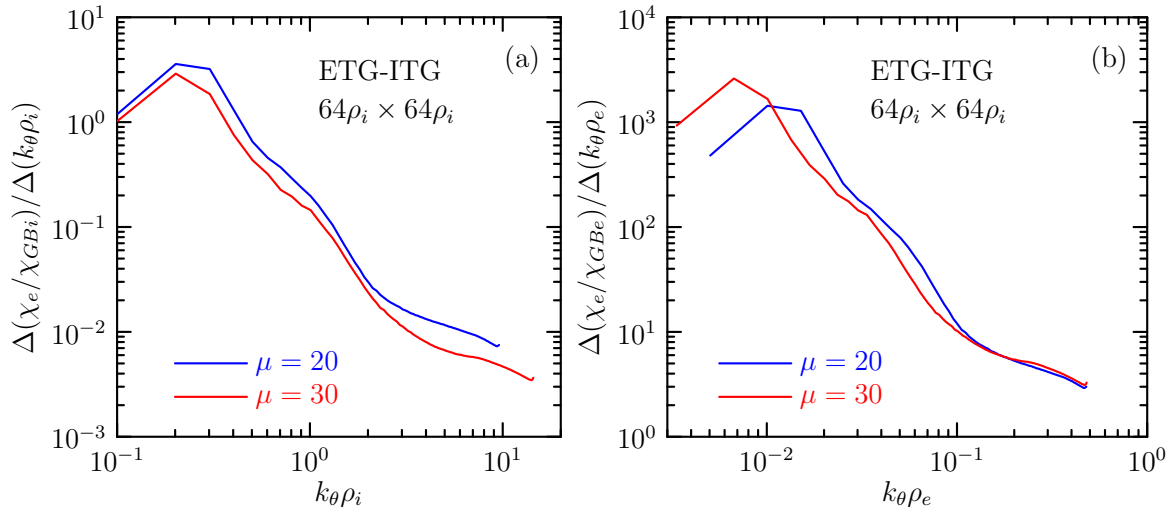
FIG. 7. (a) Transport as measured in ion units. A drop in electron energy transport is seen in moving from $\mu = 20$ (blue curve) to $\mu = 30$ (red curve). (b) However, when measured in electron units, the universality of the transport for $k_\theta \rho_e > 0.1$ becomes apparent.

5. Acknowledgement

References

[1] DORLAND, W. et al., Phys. Rev. Lett. **85** (2000) 5579.

[2] JENKO, F. et al., Phys. Plasmas **7** (2000) 1904.

[3] JENKO, F. et al., Phys. Rev. Lett. **89** (2002) 225001.

[4] DIMITS, A. et al., Phys. Plasmas **7** (2000) 969.

[5] NEVINS, W. et al., Phys. Plasmas **12** (2005) 122305.

[6] CANDY, J. et al., J. Comput. Phys. **186** (2003) 545.

[7] CANDY, J. et al., Phys. Plasmas **13** (2006) 032310.

[8] ESTRADA-MILA, C. et al., Phys. Plasmas **12** (2005) 022305.

[9] CANDY, J., Phys. Plasmas **12** (2005) 072307.

[10] WALTZ, R. et al., Phys. Plasmas **12** (2006) 052301.

[11] HOLLAND, C. et al., Phys. Plasmas **11** (2004) 1043.